Observing Distal Volcanic Ash Evolution Using Optical Flow Algorithms

Project Number: AO18
Candidate Number: 1043237
Supervisors: Dr A Prata and Prof R G Grainger

Abstract. In volcanic eruptions, volcanic ash can be ejected several kilometres high into the atmosphere, where it is transported and dispersed by winds. Numerically modelling ash dispersion is crucial for aviation safety because ash has the potential to damage flight-critical infrastructure on aircraft [1][2]. The development of these numerical models relies on observations of how ash evolves over its lifetime. Thus, this project aims to make such targeted observations using satellite images. Existing techniques to measure ash cloud properties are combined with 'optical flow' algorithms which track ash particle motion. This produces real-time data on how ash particles are removed from the cloud. In the first method, ash cloud properties are observed in a 'Lagrangian' reference frame moving with ash particles. In the second method, changes to the ash cloud caused by depositional processes are isolated in the observations. These methods are applied the July/August 2020 eruption of Nishinoshima, Japan.

I. INTRODUCTION

During volcanic eruptions, Volcanic Ash Advisory Centres (VAACs) are responsible for issuing ash forecasts and no-fly zones [3]. These are produced using numerical models which simulate ash transport (the following discussion is based on the model used by the London VAAC, called NAME [4]). These models consider how individual ash particles are transported by the wind, as well as how they interact with each other and their environment. The interacting processes come in two main types: particle aggregation, where smaller particles stick together to form larger, heavier particles [5], and particle washout, where ash is removed from the cloud by ice or liquid water in the form of 'hydrometeors' [6]. In models, these processes are represented with parametrizations because too many particles are involved on too small a scale to simulate explicitly. However, not all of these processes are included in current dispersion models. For example, NAME does not consider aggregation [4]. This introduces some error to ash forecasts, since aggregated particles typically have different terminal velocities from their constituents, so their predicted times spent in the ash cloud before fall-out will differ [5].

To develop and validate model parametrizations, observations are required of these processes in action. The only observations which have sufficient spatio-temporal coverage and resolution come from satellite platforms, since clouds of 'distal' ash can travel thousands of kilometres before being deposited [7] (distal ash is small enough that it is carried passively by currents of air. It is typically smaller than 15 µm). Prior studies have developed satellite 'retrieval' techniques, which use the physics of how ash and its environment interact with infrared (IR) radiation to obtain the properties of ash clouds from satellite images [8][9][10].

Meanwhile, in separate studies of water clouds, detailed observations have been made of how the properties of those clouds change over their lifetimes [11][12][13]. This was achieved by tracking clouds in satellite images, sometimes by using 'optical flow' algorithms which calculated the cloud velocities.

Thus, this project combines satellite retrieval data of ash cloud properties with optical flow-derived estimates of ash velocities in satellite images. In section IV B, the motion vectors are used to track distal ash particles within an ash cloud, and their properties are studied over time in the co-moving ('Lagrangian') frame of reference. These observations are used to study ash particle dynamics, but only with limited statistical power. Hence, the ash velocities are also used to model the changing masses of larger swaths of the cloud. These models are used to quantitatively test simple parameterizations of ash particle evolution (sections IV C and IV D).

These methods were applied to a single case study: the July/August 2020 eruption of Nishinoshima, a Japanese volcanic island. Section II presents the satellite data used. Section III describes how the properties of volcanic ash and its 2D motion field were estimated from this data. Section IV explains the methods introduced above and presents their results. Finally, section V considers how this study could be improved and its results applied.

II. DATA

A. Advanced Himawari Imager

The satellite data for this project came from the Advanced Himawari Imager (AHI), an imaging radiometer onboard the Himawari-8 geostationary satellite (imaging radiometers look at the Earth's surface and take 2D images of the radiance in different bands of the EM spectrum. Radiance is the power radiated by a body in a unit frequency interval and unit solid angle). AHI has IR bands centered at 10.4, 11.2, 12.4 µm. These record an image every 10 minutes at 2 km resolution at nadir (the viewing point directly below the satellite, where the finest image resolution is). This project used the data from these bands in a window surrounding Nishinoshima from 31/07/2020 00:00 - 02/08/2020 00:00. Sometimes the raw AHI data was used (section III D), but sometimes it was pre-processed to convert it to equivalent brightness temperatures (sections III A and III B). A brightness temperature (BT) is the temperature of a black body which produces the same observed radiance at a given frequency.

III. METHODS

A. Ash detection flag

Before the satellite retrieval algorithm was applied to the AHI data, the data was filtered using an ash-detection routine. Then, the algorithm was only applied to those pixels flagged as containing ash.

The detection routine uses the fact that, between 10-12 µm, ash emissivity increases with wavelength, while water and ice emissivity decrease [14]. Thus, if there is a sufficient quantity of ash within a pixel, the observed brightness temperature should increase with wavelength between 10-12 µm. Hence, the detection routine calculated the pixel-wise brightness temperature difference (BTD) between the 10.4 µm and 11.2 µm channels from the AHI data. If this quantity was negative, the pixel was flagged as containing ash.

B. ORAC retrievals

The satellite retrieval data for this project was calculated by the Optimal Retrieval of Aerosol and Cloud (ORAC) algorithm. Here, a necessary overview of the algorithm is given, but [8] is referred to for a more in-depth discussion.

To estimate the physical properties of ash clouds from satellite images, ORAC first makes a simplifying assumption. It assumes that all light reaching a pixel in the satellite sensor travels straight from the atmospheric column lying underneath that pixel. This allows the model to be run independently on each pixel. It also means that the output has an intuitive interpretation; each pixel represents a columnar cloud whose properties are being observed. This set of properties is called the cloud 'state'.

ORAC then simulates what clouds with different possible states would look like from a satellite's perspective. This simulation uses ORAC's 'forward model', a simplified model of radiative transfer in the Earth's atmosphere which represents the cloud as a geometrically infinitesimally thin layer. Finally, ORAC finds the cloud state which minimises the difference between the simulated cloud radiances and the observations. This is its best estimate of the true cloud state.

The retrieved state vector contains the cloud top height (H), optical thickness (τ, dimensionless), effective particle radius (r_e), and sea surface temperature below the cloud (T_s), along with uncertainties on these quantities. Optical thickness described the attenuation of a 550nm beam of light passing vertically through the whole cloud thickness, as in (1) (L_{in} is the radiance entering at the cloud base, L_{out} is the radiance exiting the cloud top). Note that if $\tau > 1$, most radiation will be absorbed as it passes through the cloud. Then, most of the radiation received in space will be that emitted by the ash, not that coming from the ground.

$$L_{out}/L_{in} = e^{-\tau} \tag{1}$$

$$r_{eff} = \bar{r^3}/\bar{r^2} \tag{2}$$

The effective radius is a statistical measure of the average ash particle size, calculated as in (2) (barred quantities are averages over all particles).

C. ORAC mass-loading

From the retrieved cloud properties, ORAC also estimates the mass loading (m$_l$, the ash mass contained within each unit area of a cloud when viewed

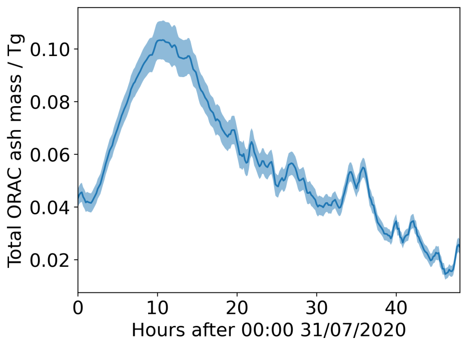

FIG. 1. Total ash mass retrieved by ORAC from AHI data. Two periods of net mass increase are observed, between 02:00-11:00 07/31/2020, and 09:00-11:00 08/01/2020.

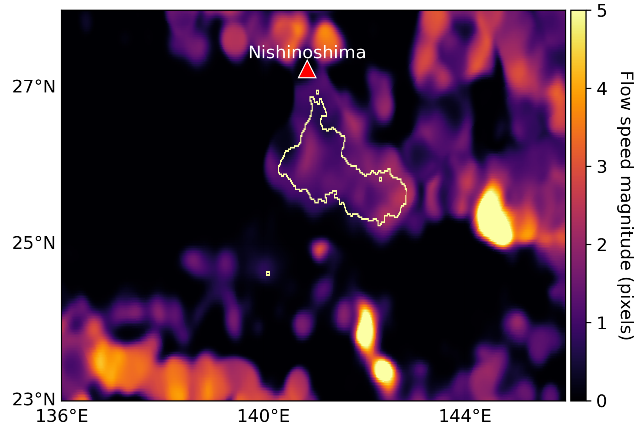

FIG. 2. The calculated magnitudes of optical flow vectors are shown on a latitude-longitude grid at 07:00 31/07/2020. The flow was derived from images of the $11.2 - 12.4\,\mu m$ AHI radiance difference. The ash-flag boundary is shown in white. The ash motion is clearly identified. Overall, flow vectors near the cloud point southwards. Other features are also seen in motion, most likely water clouds.

from above). ORAC assumes a constant ratio between the optical extinction cross-section and geometric cross-section of ash particles, Q_{ext}. Thus, the total geometric ash cross section per unit ash cloud area is τ/Q_{ext}. Assuming all particles are spheres with radius r_e and density ρ, spherical geometry gives (3). A formal derivation is available in [15].

$$m_l = \frac{4\tau r_e \rho}{3Q_{ext}} \tag{3}$$

Integrating the mass loading over the ash cloud area gives the total mass in the scene (figure 1). Two periods of net mass increase were observed. These occurred when there was significant eruptive activity from Nishinoshima, the only ash source.

D. Optical flow algorithms

In section I, it was mentioned that, by combining observations of ash cloud properties with the ash motion field, one could study ash particles over their lifetimes. This approach was prompted by the use of 'optical flow' techniques in other studies to track and study water clouds [13].

The purpose of optical flow algorithms is to estimate the apparent displacements of objects between images, using the differences in pixel intensities. In this project, we want the optical flow field which is derived to represent the horizontal motion of particles in the ash cloud. However, there is one issue with this. The cloud is made of layers of microscopic particles, whose velocities differ over the thickness of the cloud. But, from a satellite image, we can only derive a two-dimensional flow field. Thus, optical flow algorithms can only derive ash particle displacements accurately if these do not differ greatly over the cloud thickness. This condition might not generally hold, so sections IV C and IV D will consider how well it is met. In the meantime, to develop the methods of the following sections, we will assume that it holds.

Other caveats come from considering the optical flow algorithm itself. This project used the 'Farnebäck' algorithm [16] because of its proven utility in tracking water clouds in geostationary satellite images [13]. It is a 'dense', 'local' algorithm, meaning that it estimates the optical flow at every pixel in an image, and does this by matching correlated local patterns of intensity between subsequent images. Numerically, the algorithm first considers a region around the pixel whose flow is required. It then displaces this region by some vector and calculates the sum-of-squares difference between it and the pixels it lands on. It repeats this systematically for many displacements, and takes the one yielding the lowest difference as the estimate for the flow vector.

From this discussion, we infer that, if an ash cloud moves horizontally over a uniform sea surface (so any changes in radiance come from the cloud alone) and the particle velocity is uniform over the cloud thickness, then the optical flow field will correspond precisely with the physical motion of ash particles. Between two images of the cloud, the particles either move by the optical flow displacement or are lost to depositional processes.

One flow field from this study is shown in figure 2. The ash cloud motion is clearly detected; the flow contours match the flagged cloud shape well. As an initial test, this suggests that the Farnebäck algorithm worked to track ash motion.

In the following sections, optical flow displacements will be discussed using the notation below. At each time t and point in space $\mathbf{x}$, an optical flow vector, $\mathbf{f}_{\Delta t}$, has been derived from two images separated by a time interval Δt. A corresponding map is defined to act on $(t, \mathbf{x})$, denoted $\mathbf{F}_{\Delta t}$ (4). This map represents the algorithmic best guess of how the ash at $\mathbf{x}$ moves over the interval Δt.

$$\mathbf{F}_{\Delta t}(t, \mathbf{x}) = (t + \Delta t,\ \mathbf{x} + \mathbf{f}_{\Delta t}(t, \mathbf{x})) \tag{4}$$

The equivalent, compound calculation for n timesteps is expressed in (5) (the symbol $\Delta^{(n)}$ denotes the change in a quantity over n AHI intervals).

$$\mathbf{G}_{\Delta^{(n)}t}(t, \mathbf{x}) = \mathbf{F}_{\Delta t_n}(\mathbf{F}_{\Delta t_{n-1}}(...(\mathbf{F}_{\Delta t_1}(t, \mathbf{x}))...)) \tag{5}$$

$$\Delta^{(n)}t = \sum_{i=1}^{n} \Delta t_i \tag{6}$$

IV. ANALYSIS AND RESULTS

A. Ash detection flag and ORAC retrieval data

Before attempting to study ash cloud dynamics, it is worth taking time to assess the accuracy of the ash-flag and ORAC retrieved cloud properties. This is done by comparing these datasets with independent observations of the same eruption.

First, to assess the ash detection flag, we compare the flag used in this study with a flag evaluated on data from the MODIS instrument (see figure 3. MODIS is another imaging radiometer on a polar-orbiting satellite). Both flags used the same basic method, but the MODIS flag took an additional step to account for water vapour [17]. This is probably why it detected a much larger ash area, leading to it observing more than twice the total mass of the retrieval in this study (figures 3 and 1). Figure 3 also shows that the AHI flag did not have a simple ash mass loading threshold. Some higher mass loading parts are missed, while lower parts are flagged. This

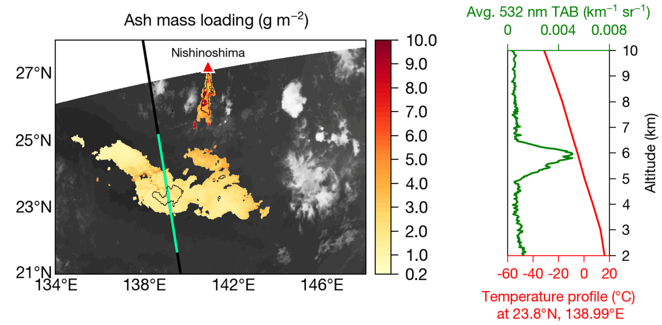

FIG. 3. Independent observations of the Nishinoshima eruption. Figures provided by Andrew Prata [18]. Left: Retrieval of mass loading at 01/08/2020 04:05, using data from the MODIS instrument. Ash is shown in yellow and orange. The total retrieved ash mass was 0.2 ± 0.1 Tg. The ground track of the CALIPSO satellite is overlaid as a black and green line. The AHI ashflag is outlined in black. Right: TAB is a measure of how much light is backscattered to CALIPSO over the green section of its track. It is plotted as a dark green line. The peak at 6 km in altitude is caused by the ash cloud [19].

issue affected the results of section IV D, as discussed there.

To assess the ORAC estimates, figure 4 shows the median values of some key ash cloud properties, evaluated across all ash-flagged pixels in the scene at each time. One observation is that the cloud optical thickness remained mostly between 1-3 over both days. This will have affected how well ORAC performed, since the forward model assumed that the cloud was an infinitesimally thin layer in the atmosphere. If $\tau \lesssim 1$, this approximation clearly breaks down, since the observed radiation would come from points over the whole cloud thickness (usually ~ 1 km). Since we are near this limit, the retrieval values may be spurious.

ORAC also estimated the cloud top height to be around 1-2.5 km on 31/07/2020, and around 2-3 km on 01/08/2020 (figure 4). These estimates can be checked against independent observations from CALIOP, a Lidar instrument onboard the CALIPSO satellite [20] (Lidar detects objects by timing the backscatter of a pulsed light beam). CALIOP actively measures the presence of aerosols (small atmospheric-borne particles), so is assumed to give the ground-truth ash cloud position. It observed the cloud top height to be around 6km at 04:05 08/01/2020 (figure 3), lying significantly above the upper quintile of ORAC cloud top heights. It is likely that this discrepancy was caused by the op-

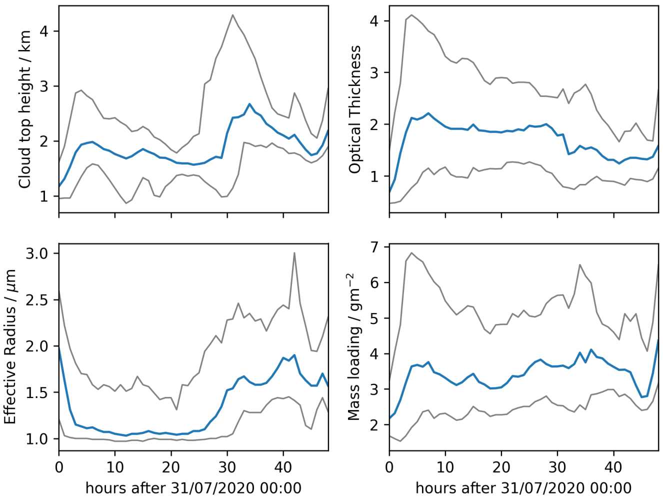

FIG. 4. Median values of ORAC retrieval parameters, evaluated over all ash-flagged pixels at a given time, are shown as solid blue lines. The upper and lower quintiles are marked in grey.

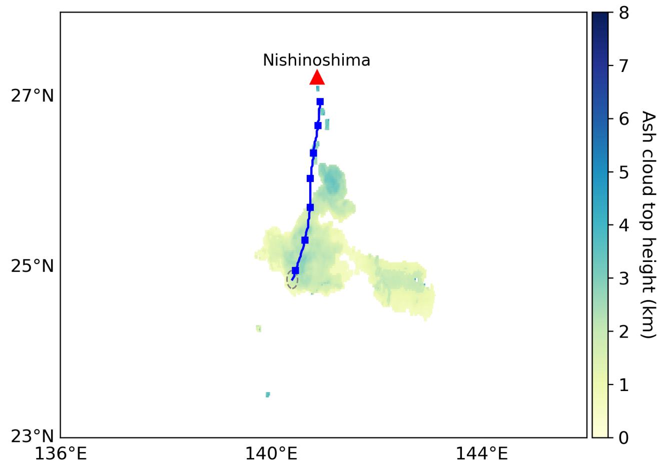

FIG. 5. An ash particle trajectory generated using optical flow fields is shown in blue, overlaid on an ORAC retrieval of cloud top height. White pixels contain no detectable ash. This trajectory was initialised at 31/07/2020 00:00; its path up to 13:00 on the same day is shown. The square markers are spaced by 2-hour intervals. The dashed grey ellipse borders the sample area for measuring ash properties at this time.

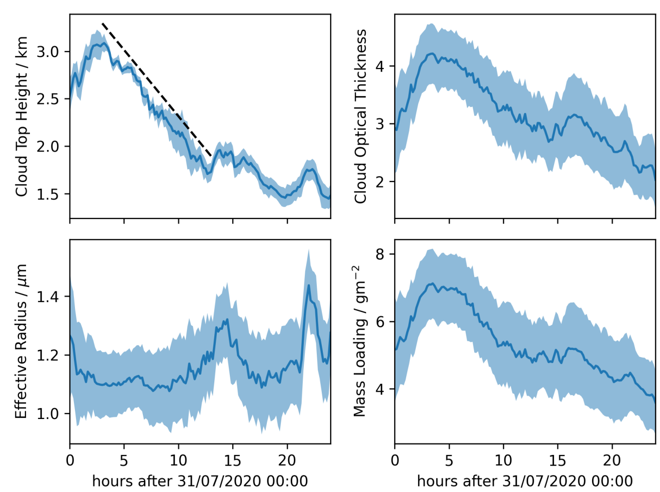

FIG. 6. Ash cloud properties sampled along a trajectory, a snapshot of which is shown in figure 5. The standard errors are shown as shaded bands. On the cloud top height plot, the dashed black line has the linear best-fit gradient for the data from 03:00 - 13:00.

tical thickness issue just described. This connection between optical thickness and cloud top height is discussed further in the next section.

B. Lagrangian observations of ash particles

In the next three sections, the retrieval data and optical flow fields are combined to observe ash particle evolution. In this first section, observations are made in the frame co-moving with ash particles.

First, the trajectory of an ash particle is generated by starting at a chosen point, then moving passively with the optical flow field. Computationally, this is achieved by applying the map defined in (5). The resulting trajectory is shown in figure 5. Every ten minutes, the ash cloud properties were sampled and averaged in a region surrounding the trajectory location. This was done instead of taking a single-pixel reading to acknowledge the uncertainty in the trajectory position, and also to reduce the uncertainty inherent in the ORAC retrievals (this is valid since the cloud properties should not vary greatly across the sample region). The results are shown in figure 6.

In figure 6, the effective radius (r_e) stays roughly constant at 1.1 μm, increasing briefly around 14:00 and 23:00. Physically, particle fallout would have acted to decrease r_e, since larger particles have higher terminal velocities, so fall out more quickly, while aggregation of particles would have increased r_e. However, aggregation would not have caused both observed increases in figure 6, since it would only affect the particle size distribution once, and over a longer timescale than one hour. It is more likely that the effective radii retrieved by ORAC were spurious. In fact, that the effective radius stayed roughly constant suggests that ORAC may not have had sufficient information to accurately retrieve this variable. This is not wholly unexpected, since ORAC was used to estimate four cloud state variables, but was only provided with data from three spectral channels (section III B).

The low variation of the effective radius explains another trend in the observations. By holding r_e constant in the calculation of the mass loading (3), the mass loading becomes proportional to the optical thickness, as observed.

Also in figure 6, the changes in cloud top height and optical thickness are correlated. Again, this is probably caused by ORAC's modelling assumptions and the data it was provided. As the cloud optical thickness decreased, more radiation would have reached the satellite from altitudes below the true cloud top. Since ORAC assumed that the ash cloud was geometrically infinitesimally thin, it would have placed the cloud at a lower altitude to account for this excess radiation (in the troposphere, the atmospheric layer where the cloud resides, air at lower altitudes is warmer, and warmer bodies emit more radiation). These factors also lead to a faster cloud top height fall rate than is physical. Between 03:00 - 13:00, $\frac{DH}{Dt} = -3.9\,\mathrm{cm\,s^{-1}}$ ($\frac{D}{Dt}$ is the Lagrangian derivative: the rate of change in the frame moving with the ash). This corresponds to the terminal fall speed of particles with diameter $\sim 20\,\mu\mathrm{m}$, or aggregates of up to $100\,\mu\mathrm{m}$ [21]. While we expect there to be some particles of these sizes in the first day after eruption, there would also be some remaining fine ash which would descend more slowly, giving a slower $\frac{DH}{Dt}$ in reality.

Now, the known biases in the retrieval data have been considered, but there remains one spurious feature in figure 6. In the first few hours, the cloud optical thickness increases significantly. This is physically unexpected, and could indicate that the optical flow technique does not work to track individual ash particles. If this feature persists when this study is repeated with reliable retrievals, then the assumptions in section III D will be strongly in doubt.

Clearly these issues mean that the timeseries in figure 6 should be interpreted with some caution. However, after 05:00, H, τ, and m_l all decrease monotonically, as is expected physically (there are some bumps in H, τ, but these are not significant). Hence, it is possible that, for distal ash further than about 50 km from the volcano, the optical flow algorithm did accurately derive ash motion and this method of Lagrangian tracking works. If this is the case, then repetition of this study with reliable retrievals should permit quantitative physical insights to be made. Unfortunately, the issues mentioned mean that this is not currently possible.

C. Global mass balance

In this section, an alternative method of analysing ash particle evolution is developed. It considers all ash-flagged pixels in the scene, so has greater statistical power than the single-trajectory study of the previous section.

The method uses the fact that, with the optical flow field, one can match ash-containing pixels in one satellite image with their counterparts in the previous image. The change in ash properties between these pixels tells us how this ash evolved over the time between the two images. If we parametrize this evolution, then we can attempt to explain the observed change in mass of the ash cloud in terms of individual physical processes. Thus, this method first derives a complete model of how the total ash mass changes over time. This model is then fit to the observations. Finally, the goodness of this fit is used to measure the accuracy of the parametrizations employed and the parameter values obtained.

This method can be applied to any mass distribution. However, we know that its quantitative results in this project will be inaccurate, because they rely on an inaccurate retrieval dataset (sections IV A and IV B). Thus, only simple parametrizations will be used, just to determine whether it is worth repeating this study with more accurate data.

To begin, note that at time t, The total observed ash mass, M_{obs}, is given by the sum of the ash masses per pixel, m, in all the ash-flagged pixels (section III A). These pixels are indexed by the set $i(t)$.

$$M_{obs}(t) = \sum_{i(t)} m(\mathbf{x}_i) \tag{7}$$

Evolving to the some later time, $t + \Delta^{(n)}t$, the existing ash will disperse horizontally, spreading over a larger area, causing the mass loading to decrease (by mass conservation). Since the ash-flagging procedure cannot detect arbitrarily small mass loadings, some of this ash will be missed. It is assumed that this ash continues dispersing at later times, so is not detected again. To estimate the size of this contribution, it is assumed, as usual, that all ash particles move passively with the optical flow field. Formally, the flow field maps the ash-flagged set, $i(t)$, to a new set, $i'(t+\Delta^{(n)}t) \equiv \mathbf{G}_{\Delta^{(n)}t}(i(t))$, where $\mathbf{G}_{\Delta^{(n)}t}$ is defined in (5). Then, under the stated assumption, any points in $i'(t+\Delta^{(n)}t)$ that are not in the ash-flagged set $i(t+\Delta^{(n)}t)$ have missed detection; their ash content dispersed below a critical mass loading. The corresponding subset of $i(t)$ is denoted $l(t)$, the pixels whose mass was 'lost' over the time interval. The other pixels in $i(t)$ are denoted as $r(t)$, the set of points remaining in the cloud. Figure 8 shows $l(t)$, $r(t)$ in red, green respectively.

The mass of the ash which remained in the cloud (in the set $r(t)$) will have been affected by depositional processes, like washout or aggregation-enhanced fallout. The action of these processes was parametrized using the scheme (8). It works like a scavenging coefficient [22]: Λ removes a constant fraction of the ash mass within a pixel, m, per unit time, as that ash is in motion.

$$\frac{Dm}{Dt} = -\Lambda m \tag{8}$$

Meanwhile, there is ash being erupted by the volcano. This is represented with a source term in the model, equal to the mass eruption rate (MER) of fine ash (only fine ash is optically retrievable in the IR). First, the so-called Mastin relationship [23] (equation (9)) was considered as it is commonly used in numerical models (e.g. [4]). It estimates the total MER of ash particles of all sizes, $\dot{M}_e$, in terms of the height above the volcano at which the ash horizontally disperses, H, and two constants. The value $b = 0.25$ was chosen, consistent with [23] and [8], and H was taken to be the maximum observed cloud top height near the volcano (a good estimate when $H < 10\,\mathrm{km}$ [23]). Unfortunately, this term proved too erratic to be used (figure 7(b)). When included in a provisional model, the large peak at 30-35 hours dominated the fitting process. Thus, since the source term varied little aside from the peak, it was simply approximated as a constant, $\dot{M}_e = c$. Interestingly, the peak was probably physical, being caused by the coincident volcanic activity observed in figure 1. However, that figure would also indicate that a peak between 2-10 hours was missed, where volcanic activity was also high. This may have been because the ash flag did not have a consistent mass loading threshold, so could have missed the relevant, higher altitude part of the cloud (section IV A).

$$\dot{M}_e = aH^{1/b} \tag{9}$$

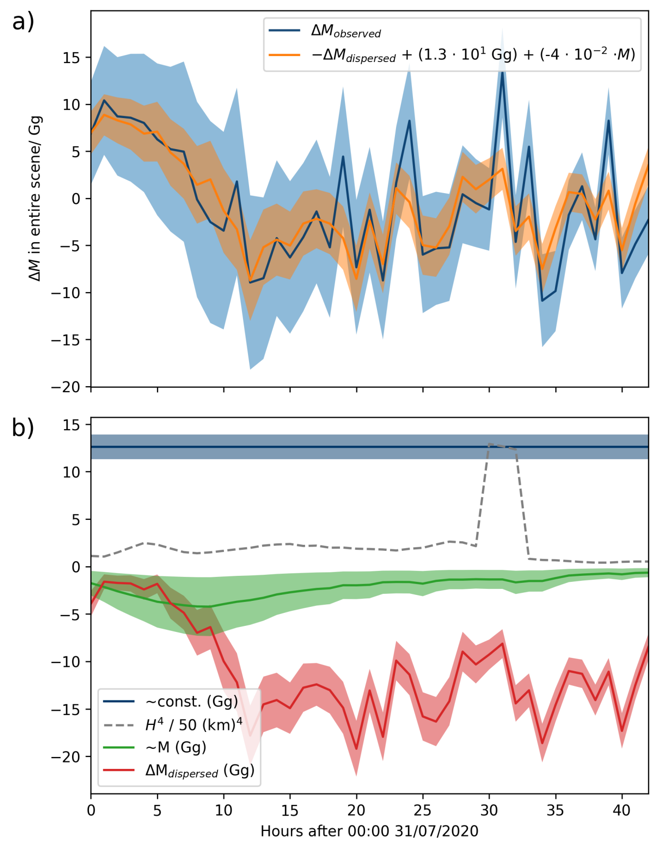

FIG. 7. Modelling the observed mass change across the whole scene. 7(a) The observed mass changes over 1-hour intervals are shown in blue, the model is in orange. The model is (10). The parameters give the least squares fit to the observations. For the model and data, $\chi^2 = 96$. Since $P(\chi^2 > 96 \mid \mathrm{df} = 41) = 3 \times 10^{-6}$, the model is a poor fit to the data. However, for the first 30 hours, $\chi^2 = 24$. Since $P(\chi^2 > 24 \mid \mathrm{df} = 28) = 0.69$, the fit is only poor at later times. 7(b) The additive terms in the model are plotted as bold lines. The dashed line is proportional to the proposed Mastin source term (9).

Overall, this gives a model for the change in the total observed mass over n AHI image intervals (10). There are two free parameters: c and Λ.

$$\begin{aligned}\Delta^{(n)} M_{obs} = &- \sum_{l(t)} m(\mathbf{x}_l) + c\,\Delta^{(n)}t \\ &- \Lambda \Delta^{(n)}t \sum_{r(t)} m(\mathbf{x}_r)\end{aligned} \tag{10}$$

The observed mass changes in the scene and the least-squares fitted model are presented in figure 7(a). Overall, the model captured the 5-hourly trends well but, after 21:00 31/07/2020, it failed to recreate the large, roughly hour long, fluctuations in the observations. This was likely caused by the

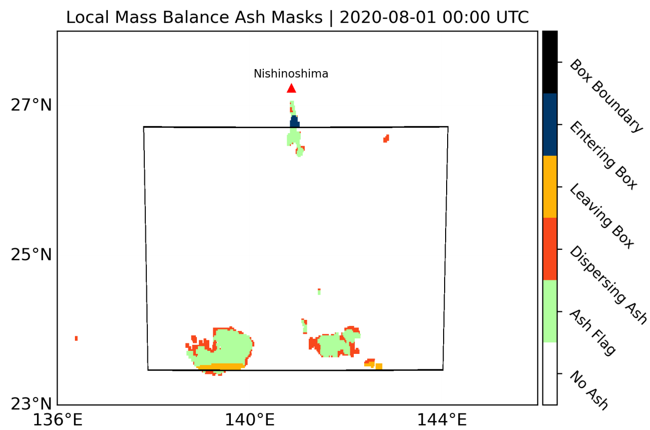

FIG. 8. Flagged regions corresponding to ash entering the boxed domain (blue), leaving the boxed domain (yellow), dispersing at the edges of the cloud (red), and in the bulk of the cloud (green).

crude modelling of the source term. If a more sensitive ash flag had been used, a Mastin source term could have been constructed, possibly accounting for the missing variation. The fitted model parameters were $c = (13\pm1)\,\mathrm{Gg\,hr^{-1}}$ and $\Lambda = (4\pm3)\times10^{-2}\,\mathrm{hr^{-1}}$. This gives the e-folding time for the true mass of the ash cloud, $t_e = \Lambda^{-1} = (20\pm10)$ hours. This value is consistent with eruptions of other volcanoes [8] so, despite the spurious retrieval data, is not unphysical.

D. Source-free mass balance

In the previous section, it proved difficult to obtain an accurate MER. Thus, this section extends the model of the previous section by omitting the volcanic source term. This is achieved by only considering changes within a region, S (outlined in black in figure 8), which excludes the volcano. Instead of the source term, the net mass flux into/out of S is calculated. To do so, the sets $\alpha(t)$ and $\beta(t)$ are defined as those points which, under the optical flow map (5), enter S from outside and leave it from inside respectively ($\alpha(t)$, $\beta(t)$ are shown in blue, yellow in figure 8). The sets $r(t)$ and $l(t)$ are the same as in the previous model, except they only include those points which remain within S over the whole time interval. Overall, this gives a model for the mass change inside S over n AHI intervals (11).

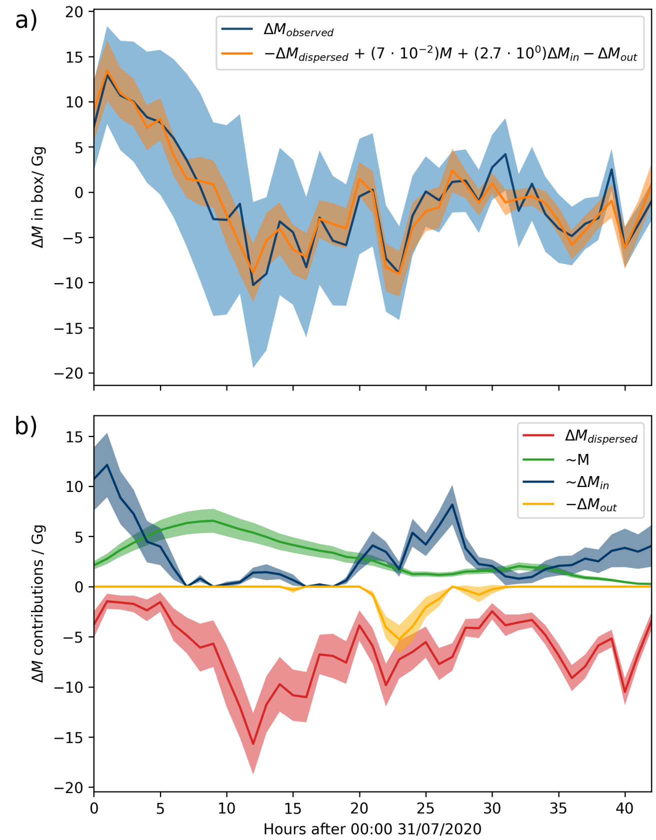

FIG. 9. Modelling the observed mass change over 1-hour intervals in the region outlined in figure 8. The 1-hour interval was chosen to give optical flow displacements several pixels long, so it was clear whether particles had crossed the boundary of S. (a) Observations are shown in blue, the model is in orange. The model is (11), with the parameters giving the least squares fit to the observations. The model and observations gave $\chi^2 = 39$. Since $P(\chi^2 > 39 \mid \mathrm{df} = 41) = 0.56$, the model is not a bad fit to the data. (b) The additive terms in the model.

$$\begin{aligned}\Delta^{(n)} M_S = &-\sum_{l(t)} m(\mathbf{x}_l) - \Lambda\Delta^{(n)}t\sum_{r(t)} m(\mathbf{x}_r)\\ &+ A\Delta^{(n)}t\sum_{\alpha(t)} m(\mathbf{x}_\alpha) - \sum_{\beta(t)} m(\mathbf{x}_\beta)\end{aligned} \tag{11}$$

The $\alpha(t)$ term is multiplied by an unknown parameter, A, because the ash entering S will lose mass like the rest of the cloud as it travels. If these losses are spatially uniform, we expect $A = 1 - \Lambda$.

Figure 9 shows the observed values for $\Delta^{(n)}M_S$ and the least squares fit of the model. The optimal parameters were $\Lambda = (-6\pm1)\times10^{-2}\,\mathrm{hr^{-1}}$ and $A = (2.6\pm0.2)\,\mathrm{hr^{-1}}$. Unfortunately, Λ was negative, and A was greater than one. Both values suggest that the mass of an isolated ash cloud would increase, a process for which there is no physical mechanism. This is not an unexpected result since, in section IV B, the sampled mass loading initially increased along an ash particle trajectory. Nonetheless, it means that the model cannot be interpreted in the way it was designed to be, so cannot be used to make any physical insights. Despite this, it is encouraging that the model fit the data well, and that the optical flow-derived mass fluxes accurately accounted for most of the short-term variation in the observations. This suggests that the method works, and that it is worth repeating with more accurate retrieval data.

It should also be noted that the ash flag issues mentioned in section III A may have contributed to the unphysical result. The flag did not have a simple mass loading threshold, so as regions of the cloud dispersed, they may have become detectable where previously they were not. It would thus seem like mass was appearing with no source, as observed.

V. CONCLUSIONS

This report has presented an application of optical flow algorithms to derive volcanic ash motion from geostationary satellite images. This was implemented in three methods to observe ash cloud dynamics, which were applied to the 31/07 – 01/08/2020 eruption of Nishinoshima. The methods showed promise, producing realistic particle trajectories and modelling ash cloud mass balances well. However, with the retrieval data currently available, no novel insights could be made into the physics of ash cloud evolution.

First, the ORAC retrieval dataset was compared to independent observations to check for errors. Unfortunately, the cloud was optically thin ($\tau \lesssim 3$), which meant that the retrieved cloud top height did not agree with independent Lidar observations. This issue could be dealt with by modifying the thin cloud assumption in ORAC's forward model. Namely, it may be possible to model a cloud with finite thickness as an infinitesimally thin cloud with modified emissivity. Implementing this is a current aim for ORAC's future development [24].

In the first optical flow-based method, ash cloud properties were studied along a particle trajectory from the first day of observations. With the retrieval data used, the mass loading increased during the first few hours; this result has no physical explanation if the particle trajectory was accurate. Thus, in future work, more accurate retrieval data should be used. This would hopefully address the unphysical result. If it does not, then the assumptions made about ash cloud dispersion (section III D) would be brought into doubt, as these determine how suitable optical flow algorithms are for tracking ash particle motion. Also in the retrieval data, the variation in the effective radius was unexpectedly small. More information on this quantity could be obtained by including an additional spectral channel in the ORAC input (as done in [8]).

The other optical flow-based methods attempted to model the changing mass in parts of the ash cloud, aiming to test simple parameterizations of ash evolution. The larger datasets involved made these methods more powerful quantitative tools. The first model considered the mass changes across the whole scene. It assumed a constant mass eruption rate from the volcano and, using the optical flow field, computed which parts of the cloud escaped the detection algorithm in each time interval. This model was successful for the first day of observations. The 5-hourly variation in the observed masses was described well by the detection losses, and the bulk ash mass had an e-folding time of 20 ± 10 hours, comparable to that observed in other eruptions. However, in the second day, large, roughly hour-long, fluctuations in the total mass change were missed by the model, likely because of the crude source term approximation used. If a more sensitive ash detection method was available, a source term instead could be constructed based on the Mastin relationship.

So that the volcanic source term could be ignored, the final method modelled the mass balance in a bounded region of the scene. This model fit the observations well but, when physically interpreted, required the presence of unexpected mass sources. This was most likely caused by the increasing mass loading along optical flow trajectories which was noted earlier. Also, the simple ash detection routine may have contributed to this error. Thus, future studies should use an ash flag with known mass loading limits, and only apply it where mass loadings lie below the upper detection limit.

The optical flow techniques could possibly also be improved. The Farnebäck optical flow algorithm was chosen because it had previously been used with satellite observations of water clouds [13]. However, that study did not test whether it was the optimal algorithm to use. One could test different algorithms by applying them to simulated satellite data, evaluated on an ash dispersion model. Then, the agreement between the optical flow field and known particle motion could be tested.

By repeating these analyses with the suggested improvements, the methods could provide high-resolution observations of distal ash physics occurring in real time. One could then introduce and test more detailed parameterizations of ash evolution. This may help to develop more accurate numerical models for operational use.

VI. ACKNOWLEDGEMENTS

The author thanks Andrew Prata (AOPP, Oxford) for running the ash flag and ORAC algorithm on the AHI data (sections III A, B, C), and providing the images in figure 3. Also, William Jones (AOPP, Oxford) for his discussions regarding the 'tobac-flow' Python package [13], which contained the implementation of the Farnebäck algorithm used in this study.

[1] Paredes-Mariño *et al.*, The lifecycle of volcanic ash: advances and ongoing challenges, Bulletin of Volcanology **84**, 51 (2022).

[2] W. Chen and L. Zhao, Review – volcanic ash and its influence on aircraft engine components, Procedia Engineering **99**, 795 (2015).

[3] ICAO, *Handbook on the international airways volcano watch* (2020).

[4] C. Witham *et al.*, *The current volcanic ash modelling set-up at the London VAAC*, Tech. Rep. (Met Office, 2020).

[5] E. Rossi *et al.*, The fate of volcanic ash: premature or delayed sedimentation?, Nature Communications **12**, 1303 (2021).

[6] W. I. Rose *et al.*, Observations of volcanic clouds in their first few days of atmospheric residence: The 1992 eruptions of crater peak, mount spurr volcano, alaska, Journal of Geology **109**, 677 (2001).

[7] W. Rose and A. Durant, Fine ash content of explosive eruptions, Journal of Volcanology and Geothermal Research **186**, 32 (2009).

[8] A. T. Prata *et al.*, Uncertainty-bounded estimates of ash cloud properties using the orac algorithm: application to the 2019 raikoke eruption, Atmospheric Measurement Techniques **15**, 5985 (2022).

[9] D. B. Williams and M. S. Ramsey, Analysis of ash emissions from the 2020 nishinoshima eruption using aster thermal infrared orbital data, Journal of Volcanology and Geothermal Research **421**, 107424 (2022).

[10] G. R. Mcgarragh *et al.*, Volcanic Ash Retrievals Using ORAC and Satellite Measurements in the Visible and IR, in *ATMOS 2015*, ESA Special Publication, Vol. 735 (2015) p. 32.

[11] T. Seelig *et al.*, Life cycle of shallow marine cumulus clouds from geostationary satellite observations, Journal of Geophysical Research: Atmospheres **126** (2021).

[12] M. Heikenfeld *et al.*, tobac 1.2: towards a flexible framework for tracking and analysis of clouds in diverse datasets, Geoscientific Model Development **12**, 4551 (2019).

[13] W. K. Jones *et al.*, A semi-lagrangian method for detecting and tracking deep convective clouds in geostationary satellite observations, Atmospheric Measurement Techniques **16**, 1043 (2023).

[14] A. J. Prata, Infrared radiative transfer calculations for volcanic ash clouds, Geophysical Research Letters **16**, 1293 (1989).

[15] S. Wen and W. I. Rose, Retrieval of sizes and total masses of particles in volcanic clouds using avhrr bands 4 and 5, Journal of Geophysical Research: Atmospheres **99**, 5421 (1994).

[16] G. Farnebäck, Two-frame motion estimation based on polynomial expansion, in *Image Analysis* (Springer Berlin Heidelberg, 2003) pp. 363–370.

[17] A. Prata, personal communication (2023).

[18] A. Prata, `https://twitter.com/andyprata/status/1290420241386876937/photo/1` (2020).

[19] S. Ahn *et al.*, Enhanced accuracy of airborne volcanic ash detection using the geokompsat-2a satellite, Sensors **21** (2021).

[20] D. M. Winker *et al.*, Overview of the calipso mission and caliop data processing algorithms, Journal of Atmospheric and Oceanic Technology **26**, 2310 (2009).

[21] A. Costa *et al.*, A model for wet aggregation of ash particles in volcanic plumes and clouds: 1. theoretical formulation, Journal of Geophysical Research: Solid Earth **115** (2010).

[22] J. Feng, A 3-mode parameterization of below-cloud scavenging of aerosols for use in atmospheric dispersion models, Atmospheric Environment - ATMOS ENVIRON **41**, 6808 (2007).

[23] L. Mastin *et al.*, A multidisciplinary effort to assign realistic source parameters to models of volcanic ash-cloud transport and dispersion during eruptions, Journal of Volcanology and Geothermal Research **186**, 10 (2009).

[24] R. G. Grainger, personal communication (2023).